PNAS
www.pnas.org

Main Manuscript for

The hemispheric contrast in cloud microphysical properties constrains aerosol forcing

Isabel L. McCoy(1)†, Daniel T. McCoy(2)†, Robert Wood(1), Leighton Regayre(2), Duncan Watson-Parris(3), Daniel P. Grosvenor(2,4), Jane P. Mulcahy(5), Yongxiang Hu(6), Frida A. -M. Bender(7), Paul R. Field(2,5), Ken Carslaw(2), Hamish Gordon(2,8)

1. Atmospheric Sciences Department, University of Washington, Seattle, WA 98105, United States

2. Institute for Climate and Atmospheric Science, Leeds LS2 9PH, United Kingdom

3. Department of Physics, University of Oxford, Oxford OX1 3PU, United Kingdom

4. National Center for Atmospheric Science, Leeds LS2 9PH, United Kingdom

5. Met Office, Exeter EX1 3PB, United Kingdom

6. NASA Langley Research Center, Hampton, VA 23681, United States

7. Department of Meteorology and Bolin Centre for Climate Research, Stockholm University, Stockholm SE-106 91, Sweden

8. College of Engineering, Carnegie-Mellon University, Pittsburgh, PA 15213, United States

†Equally contributing

* Isabel L. McCoy

Email: imccoy@uw.edu

ILM: 0000-0002-9989-0570

DTM: 0000-0003-1148-6475

LR: 0000-0003-2699-929X

DWP: 0000-0002-5312-4950

Classification

Major: Physical Sciences

Minor: Earth, Atmosphere, and Planetary Sciences

Keywords

Cloud droplet number concentration, Southern Ocean, Radiative forcing, aerosol cloud interactions, Remote sensing

Author Contributions

All authors contributed ideas and helped edit the paper. ILM, DTM, and RW planned the paper. Data analysis was undertaken by DTM, ILM, RW, LR, DWP, and YH. Writing was undertaken by ILM and DTM. PPE output was provided by LR and KC. MODIS data was provided by DPG. Emulator calculations were provided by DWP.

This PDF file includes:

Main Text
Figures 1 to 3

Abstract

The change in planetary albedo due to aerosol-cloud interactions during the industrial era is the leading source of uncertainty in inferring Earth's climate sensitivity to increased greenhouse gases from the historical record. The variable that controls aerosol-cloud interactions in warm clouds is droplet number concentration. Global climate models demonstrate that the present-day hemispheric contrast in cloud droplet concentration between the pristine Southern Hemisphere and the polluted Northern Hemisphere oceans can be used as a proxy for anthropogenically-driven change in cloud droplet number concentration. Remotely sensed observations constrain this change in cloud droplet number concentration to be between 8 and 24 cm^{-3}. By extension, the radiative forcing since 1850 from aerosol-cloud interactions is constrained to be -1.2 to -0.6 Wm^{-2}. The robustness of this constraint depends upon the assumption that pristine Southern Ocean droplet number concentration is a suitable proxy for pre-industrial concentrations. Observed droplet number concentration over the Southern Ocean reaches values typical of polluted outflows from East Asia and North America during austral summer. These high concentrations are found to agree with several in-situ data sets. In contrast, climate models show systematic underpredictions of cloud droplet number concentration over the Southern Ocean. The higher values observed there may provide an important constraint on radiative forcing globally and motivates the need for detailed process studies of aerosol and clouds in pristine environments. The hemispheric difference in observed cloud droplet number concentration implies pre-industrial aerosol concentrations were higher than estimated by most models.

Significance Statement

Enhancement of aerosol that can nucleate cloud droplets increases the droplet number concentration and albedo of clouds. This increases the amount of sunlight reflected to space. Uncertainty in how aerosol-cloud interactions over the industrial period have increased planetary albedo by this mechanism leads to significant uncertainty in climate projections. Our work presents a novel method for observationally constraining the change in albedo due to anthropogenic aerosol emissions: a hemispheric difference in remotely sensed cloud droplet number between the pristine Southern Ocean (a pre-industrial proxy) and the polluted Northern Hemisphere. Application of this constraint to climate models reduces the range of estimated albedo change since industrialization and suggests current models underpredict cloud droplet number concentration in the pre-industrial era.

Main Text

Introduction

The change in reflected shortwave radiation between the pre-industrial (PI) and the present-day (PD) due to anthropogenic emissions of aerosols, known as aerosol radiative forcing, is the leading cause of uncertainty in inferring climate sensitivity from the observational record (1, 2). A recent survey identified the dominant contributor to the uncertainty in global-mean aerosol radiative forcing as aerosol-cloud interactions (aci) in liquid clouds (3). Aerosols change the radiation reflected back to space by liquid clouds in two ways: (i) by modulating the number concentration of cloud droplets (N_d), which changes cloud reflectivity even without any changes to cloud macrostructure (4); (ii) by changing N_d, cloud microphysical processes are altered that have various impacts on cloud macro-physical properties (e.g., cloud cover or liquid water content (5)). These effects are referred to as radiative forcing due to aerosol-cloud interactions (RF_{aci}) and cloud adjustments to aerosol, respectively (6). The combined forcing from aerosol-cloud adjustments and RF_{aci} is referred to as the effective radiative forcing due to aci (ERF_{aci}). The net aerosol forcing is the sum of ERF_{aci} and a similar quantity for aerosol direct interactions, ERF_{ari}. Here, we focus on providing an observational constraint for the change in N_d and RF_{aci}. The forcing due to aerosol-cloud adjustments is uncertain in both sign and magnitude (7-13), but is expected to scale with changes in N_d (3). Narrowing the possible range of changes in N_d and resulting RF_{aci} will narrow uncertainty in ERF_{aci} and, by extension, improve our inference of climate sensitivity (1, 3).

Radiative forcing due to aerosol-cloud interactions is non-linearly dependent on the change in N_d over the industrial period (14). Natural aerosols, or aerosols in the pre-industrial state, are the largest cause of uncertainty in aerosol forcing over the industrial period (14, 15). The PD N_d is observable, but we must infer PI N_d using other means. Here, we use the pristine Southern Hemisphere (SH) (16) as a proxy for the PI and examine the contrast between the SH and the polluted Northern Hemisphere (NH) to estimate the anthropogenic perturbation to N_d. Previous studies have discussed the hemispheric contrast in cloud properties created by anthropogenic aerosol emissions in the NH. The effective radius of droplets (r_e) is smaller in the NH than in the SH (17, 18). Feng and Ramanathan (18) found that a chemical transport model driven by reanalysis meteorology was able to produce a difference in N_d between the NH and SH consistent with remotely sensed hemispheric contrasts in r_e and cloud optical depth. Boucher and Lohmann (19) used the hemispheric difference in r_e to evaluate the robustness of the RF_{aci} simulated in instances of the LMD and ECHAM global climate models (GCMs) when a prescribed relationship between sulfate mass and N_d was implemented. As in these pioneering works, we use hemispheric differences in cloud microphysics to evaluate modeled aerosol-cloud interactions. Our approach differs from previous work in the following ways. First, r_e, while readily retrieved by remote sensing, is a function of both the number concentration of cloud condensation nuclei (CCN) and the liquid water content of clouds. The differences in cloud liquid water content between hemispheres (18, 20) will weaken any r_e based constraint on hemispheric CCN difference. N_d is calculated from remote sensing retrievals of both r_e and optical depth, τ, which helps to account for cloud liquid water contributions as outlined in Grosvenor*, et al.* (21). We use N_d observations to constrain RF_{aci} because it is the key variable linking cloud microphysical and aerosol properties (22). Second, we analyze output from a large collection of GCMs designed to quantify aerosol forcing alongside a million-member ensemble from a single model that samples uncertainty in 26 aerosol processes (23). This enables us to robustly quantify and then constrain the uncertainty in the change in N_d and RF_{aci}.

Remotely sensed N_d has been shown to be reasonably unbiased in comparison with *in situ* measurements (24-29) and to agree well in both the remote Southern Ocean (SO) (30) and the NH (29). Biases between *in situ* and MODIS N_d are on the order of 1-20 cm^{-3}, depending on geographic region and boundary-layer stratification, and systematic bias does not scale strongly with N_d (27, 29, 30). The hemispheric contrast in N_d is a difference, so this should moderate the effects of any systematic biases in N_d. Our understanding of the relationship between hemispheric contrast in N_d and anthropogenic perturbations to N_d is facilitated by insight into the uncertainty in the PI atmosphere provided by GCMs. We combine analysis of structural model uncertainty from CMIP5 models participating in the Aerocom phase II project (31) and several simulations made during the development of the atmosphere-only climate model configuration, HadGEM3-GA7.1 (32) with analysis of parametric uncertainty within a perturbed parameter ensemble (PPE) in HadGEM3-GA4-UKCA. The PPE is based on 235 individual simulations in which combinations of 26 aerosol processes and emissions were perturbed (23). The output from these 235 simulations was used to train Gaussian process emulators to enable a million model variants to be generated, facilitating more robust statistical analysis (33). We show that uniting this growing confidence in observations of N_d with state-of-the-art modelling experiments directed at evaluating aci in warm clouds allows us to bound anthropogenic perturbations to N_d and RF_{aci} over the industrial period.

Results

Definition and Application of a Hemispheric Contrast

Comparing satellite-derived N_d from MODIS with Aerocom phase II and HadGEM3-GA7.1 development simulations reveals major discrepancies in N_d between GCMs and observations in the PD. GCMs consistently overestimate tropical and NH midlatitude N_d (Fig. 1a, b). GCMs underestimate summertime marine N_d poleward of 60^o in both hemispheres, especially in the SH where observed N_d increases significantly towards Antarctica (Fig. 1a, 2a). The remote SO is among the most pristine regions in the world (16) with emissions from ocean biology controlling aerosol and N_d seasonality (34, 35). The mean MODIS summertime SO N_d is near to values found in continental outflows from heavily industrialized regions (29). The NH mid-latitude has both polluted and pristine aerosol influences. The magnitude of the observed summertime Arctic N_d increase is smaller than the summertime Antarctic increase, possibly due to the closer proximity to large continental and anthropogenic sources of aerosol in the NH. While more complex to disentangle, the NH pristine aerosol has a significant seasonal cycle driven by ocean biology (36, 37). These high summertime mid-latitude values in the NH and SH are not captured by GCMs, but, as discussed below, appear in *in situ* observations of cloud condensation nuclei (CCN) and N_d, which supports its appearance in remotely sensed N_d. PPE model members show similar discrepancies compared with satellite observations although NH values are less overestimated on average (Fig. S2).

As there are no observations of pre-industrial N_d, the accuracy of modeled PI N_d cannot be evaluated directly. However, we are able to draw three qualitative conclusions regarding the PI and PD N_d from the models. First, in the GCMs the majority of the PD-PI change is in the NH. This is consistent with the zones of maximum anthropogenic emissions and direct aerosol forcing (18, 38). Second, sources of CCN over the SO are largely marine with very small contributions from continents, and levels that are mostly unchanged from the PI to the PD (16). Third, our analysis of the Aerocom phase II and HadGEM3-GA7.1 development simulations show the PI N_d is fairly similar in the NH and SH, with a difference in the 30°-60° latitude bands over oceans for these simulations of 16 ± 7 cm^{-3} at 95% confidence. In contrast, simulated PD N_d difference between these bands is 43 ± 8 cm^{-3} at 95% confidence. The larger PI N_d in the NH compared to the SH is primarily due to biomass burning emissions in the NH (39). However, the relative hemispheric symmetry in PI N_d is consistent with modelling studies of aerosol sources over oceans in the PI, where marine sources contribute a large fraction of marine CCN in both hemispheres (40, 41).

Based on our ability to observe N_d in the PD and the aforementioned inferences from GCMs, we can use the hemispheric PD N_d difference between the polluted NH and the pristine SH to gain insight into the change in global-mean area-weighted N_d between PD and PI over land and ocean ($\Delta N_{d(PD\text{-}PI)}$). We find that there is a positive correlation between $\Delta N_{d(PD\text{-}PI)}$ and the differences in marine N_d between 30°-60°N and 30°-60°S ($\Delta N_{d(NH\text{-}SH)}$) within the various GCMs examined in this study and the members of the PPE (Fig. 1c). Examination of the million member sample shows that $\Delta N_{d(NH\text{-}SH)}$ is approximately linearly correlated with $\Delta N_{d(PD\text{-}PI)}$ ($R^2 = 0.3$). The Aerocom phase II models fall within the 95% prediction interval of the best fit to the PPE sample members except for ECHAM6. This may be due to ECHAM6's imposed minimum N_d of 40 cm^{-3}, which is near the mean PI N_d in the GCMs surveyed here (Fig. 1a, b). MODIS observations put $\Delta N_{d(NH\text{-}SH)}$ between 32 and 37 cm^{-3} with 95% confidence. To agree with the observed range and the linear fit to the PPE, $\Delta N_{d(PD\text{-}PI)}$ is predicted to be 8 to 24 cm^{-3} at 95% confidence (Fig. 1c).

The $\Delta N_{d(PD\text{-}PI)}$ predicted by the HadGEM3-GA7.1 development models is on the upper end of what is predicted by the PPE. This is consistent with the stronger ERF_{aci} in GA7 model versions (-2.75 Wm^{-2} in GA7.0, -1.45 Wm^{-2} in GA7.1) compared to the weaker aerosol forcing in the GA4.0 model version used in the PPE (-1.51 Wm^{-2} on average with a 95% credible range of -2.04 to -0.96 Wm^{-2}) (23, 42). The spread of $\Delta N_{d(PD\text{-}PI)}$ observed between the PPE, Aerocom, and HadGEM3-GA7 models demonstrates the importance of examining multiple GCMs to consider structural differences. Because few of the GCMs (3 of the 8 Aerocom models and none of the HadGEM3-GA7 models) are consistent with the observations, we also demonstrate the usefulness of sampling uncertainty within a single model by using the PPE. Using the million member sample helps us to avoid the equifinality issues raised by examining a single model variant (43, 44) and produces a small subset of model variants within the observational range. Further investigation of the aerosol parameters important in this subset of member variants may help us to understand the processes that are key to producing values of N_d that are consistent with observations.

We have constrained changes in $\Delta N_{d(PD\text{-}PI)}$ using observed $\Delta N_{d(NH\text{-}SH)}$. A similar constraint can be applied to RF_{aci}. The Aerocom phase II and HadGEM3-GA7.1 development models include aerosol-cloud adjustments, so we rely on our million member sample from the PPE for this analysis. We find that the RF_{aci} is negatively correlated with $\Delta N_{d(NH\text{-}SH)}$ (Fig. 1d). We fit the relationship between RF_{aci} and $\Delta N_{d(NH\text{-}SH)}$ in the million member sample using a second order polynomial. For large values of $\Delta N_{d(NH\text{-}SH)}$, the spread in RF_{aci} from the PPE is very broad. However, when N_d is more symmetric between hemispheres, the range of RF_{aci} produced by different members of the PPE narrows. The prediction interval of the fit combined with the observed $\Delta N_{d(NH\text{-}SH)}$ constrains RF_{aci} to be between -1.2 and -0.6 Wm^{-2} at 95% confidence.

One caveat to our constraint on RF_{aci} and $\Delta N_{d(PD\text{-}PI)}$ is that our methodology may suffer from the same limitations that all single-observation constraints suffer from, which is producing an overly tight constraint (45). However, combining this methodology with other observational constraints may avoid these single observation issues (e.g. as in the multi observation constraint on ERF_{aci} in Johnson*, et al.* (45) and Regayre*, et al.* (46)) as well as help to constrain uncertainty associated with other processes in the models not captured by $N_{d(NH\text{-}SH)}$ (e.g. the aerosol optical depth constraint on RF_{ari} presented in Watson-Parris*, et al.* (33)).

Evaluating Southern Ocean N_d

The hemispheric constraint depends on the accuracy of the satellite observations of PD N_d. As noted in the introduction, MODIS N_d has been extensively validated against *in situ* measurements in the NH and parts of the SH (28-30). Because N_d observations are not as plentiful in the more remote regions of the SO, we can use other datasets to assess the quality and the believability of the surprising SO MODIS N_d pattern (Fig. 2).

The latitudinal and seasonal patterns of MODIS N_d are supported by the multi-year records of CCN from Antarctic ground sites, King Sejong Station (62°S) (47) and McMurdo Station (77°S) (48) (Fig 2, Fig S3a). Comparison of MODIS N_d within 4° of each station to the CCN station data shows matching summertime peaks and an increase with poleward latitude between King Sejong and McMurdo (Fig. S3a). Summertime CCN measured at King Sejong was classified as largely biogenic (49, 50). This is consistent with measurements taken during cruises in the SO that saw increases in CCN, biogenic pre-cursor gases for CCN (i.e. phytoplankton emissions of dimethyl sulfide or DMS which can be oxidized in the atmosphere to form pre-cursors) (51), and concentrations of small particles that grow into CCN (i.e. nucleation mode aerosols, often newly formed from biogenic pre-cursor gasses) (52) near Antarctica. The RITS campaign (53, 54) also observed a summertime increase in total aerosol concentration (including nucleation and CCN size aerosols) between its winter '93 and summer '94 cruises along the coast of Antarctica (Fig. S3 map, S3b).

We suspect that the summertime peak in N_d near Antarctica is linked to increases in biological activity as sea ice retreats in these regions. The seasonal sea ice zone's high productivity and frequent, large phytoplankton blooms (55-57) lead to enhanced emissions of biogenic CCN precursor gases. Recent observations found increased concentrations of trace gases associated with DMS oxidation in the seasonal sea ice zone (51), nucleation mode particles at ice-edge (58), and nucleation mode particles in biologically active basins near Antarctica (49, 50). We can use this connection to examine the accuracy of MODIS N_d. The 2016 ORCAS flight campaign sampled N_d over both open water and broken ice in the seasonal sea ice zone in the Amundsen and Weddell seas. ORCAS observed higher N_d over marginal sea ice than over open water (based on observations of sea ice fraction (59) interpolated to the flight track; Fig. S3c). The high N_d over marginal sea ice observed during ORCAS (median ~140 cm^{-3}) is consistent with the N_d observed during the OFCAP flights across the Antarctic peninsula (60) (Fig. S3c) and with the MODIS-observed N_d. The increase in N_d over regions with marginal sea ice is also supported by MODIS N_d over the period 2003-2015 sampled along the ORCAS flight track (Fig. 3d). Examination of the entire Southern Ocean region by MODIS shows that as the sea ice begins to retreat (October-November), N_d increases sharply over recently opened water (Fig. S4) potentially linked to increases in phytoplankton productivity.

What does pristine PD N_d tell us about GCM discrepancies in aerosol-cloud interactions?

We have demonstrated that the PD N_d hemispheric contrast is a useful framework for interpreting GCM behavior. We have also demonstrated that MODIS N_d is a reliable observation of SH N_d as well as NH N_d. We further showed that summertime mid-latitude N_d can be a factor of three smaller in GCMs than in observations (Fig. 1a, b). This leaves us with an important question: how can we use the information contained in observations of the PD pristine N_d to understand what processes are currently missing or poorly captured in GCMs? Resolving these discrepancies is important for accurately depicting aerosol-cloud interactions occurring in both the PD and PI pristine environments.

In answering this question, it is important to remember that N_d is a function of both aerosol sources and sinks. We look to the SO because it is a pristine environment where aerosol sources are analogous to the PI. However, both aerosol sources and sinks may vary across the SO (see diagram in Fig 3). Sources of SO CCN are a combination of sea spray and biogenic sources and depend upon surface and free-tropospheric physical and chemical processes (61). Sea-spray emissions vary a small amount during the year (35, 61) and are unlikely to be contributing to the striking seasonal pattern in N_d (35). The dominant contributor to biogenic CCN is thought to be DMS emissions from phytoplankton with regional contributions from primary emissions of organically-enriched sea-spray (35, 62). DMS oxidizes in the atmosphere and can eventually form sulfate, an efficient CCN (19, 34, 63-66). DMS-oxidation products (e.g. pre-cursor gases such as sulfuric acid (67) and methanesulfonic acid (68)) along with other stabilizing compounds can participate in gas to particle conversion and form new, nucleation mode aerosols (69). It is thought that these new particles nucleate between 40-70% of global CCN (70). Emissions from ocean biology influence both the SH and NH maritime N_d. North Atlantic observations show phytoplankton emissions driving marine CCN and nucleation mode seasonality (36, 37).

The primary sink of CCN is coalescence scavenging associated with the formation of precipitation (71). The rapid decrease in N_d off the coast of Antarctica may be related to enhanced precipitation scavenging associated with mid-latitude storms (Fig 3**). This idea is supported by the location of the minima in MODIS N_d coinciding with the climatological position of the SH storm track in austral summer (Fig. 2a) (72). *In situ* measurements of trace gases and aerosol number concentration indicate that the biogenic sources of CCN may be enhanced near Antarctica (51, 73) possibly resulting from a reduction in precipitation depletion, an increase in biological activity near ice edge, or a combination of these source and sink changes.

To provide quantitative assessment of the role of precipitation sinks in the Southern Ocean, we apply a simple source and sink budget model for CCN and N_d (71). The ratio between N_d and N_d computed with no precipitation loss is inversely proportional to the precipitation rate and is insensitive to the aerosol source term (see methods). Unsurprisingly, the strongest precipitation sink is in the heavily precipitating SH storm track (~50°S, see N_d decrease in Fig. 1a), and the budget model shows that coalescence scavenging drives down N_d to ~30% of the values that would occur without a precipitation sink (exact values shown in Fig. S5k-o). Poleward of the storm track, at 65°S, N_d is only reduced to ~70% of the value without a precipitation sink (Fig. S5k). This may be a reflection of MBL depth being shallower over the cold waters near Antarctica, decreasing the clouds capacity to support significant boundary layer cloud precipitation (74). The budget model also shows us that the fractional reduction of N_d by precipitation has only a weak seasonal cycle and is therefore not a major determinant of the seasonal N_d cycle over the SO region. This is consistent with the conclusion from previous studies that seasonal variability in N_d over the SO is driven primarily by biogenic aerosol sources (34, 35, 65, 75).

Based on our budget model assessment, we conclude that precipitation scavenging acts as a strong sink of CCN in the midlatitude storm track and drives the decrease in N_d equatorward of Antarctica. There is evidence that models precipitate too much in this region, possibly creating too strong a sink of N_d in the storm track in GCMs (76). Discrepancies between observed and modeled N_d near Antarctica, where precipitation sinks of aerosol are weak, indicate that aerosol production processes are not well represented in GCMs either. It is likely that the same aerosol processes important near Antarctica influence other regions of the SH that have stronger precipitation sinks. Missing or incomplete mechanisms for producing CCN near Antarctica have implications for CCN across the SH. Disagreement between modeled and observed summertime midlatitude N_d in the NH, which has similar marine biogenic aerosol sources, suggests that these model discrepancies are not relegated to the SH alone. GCMs may be additionally suffering from equifinality issues (43, 44). Thus, representation of the mechanisms leading to high near-Antarctic and summertime SO N_d as well as more accurate representations of precipitation sinks are important for advancing estimations of N_d in the PI and N_d in PD pristine regions.

What factors are leading to GCM underestimation of SO N_d? One possibility could be that GCMs do not emit enough DMS into the SO, stalling particle formation and growth processes. The amount of DMS in SO seawater and the exchange of DMS between water and air are uncertain (77). Enhancement of global DMS concentrations by 70% in HadGEM3-GA7.0 did not substantially alter SO N_d or the hemispheric contrast, $\Delta N_{d(NH\text{-}SH)}$ (Fig. 1, Fig. S1). Uncertainty in air-sea exchange processes complicates this evaluation (78). However, inclusion of more complete sulfate chemistry processes (relevant for summer CCN) and improved parametrizations of sea salt production (relevant for winter CCN) bring HadGEM3-GA7.1 N_d into closer agreement with MODIS N_d (79).

Another possible explanation for low modeled SO N_d is that new particle formation, particularly the conversion from DMS-oxidation products to condensation nuclei, is inefficient in GCMs. Observations taken at the edge of Antarctica from SO air masses have signatures of sulfate-based new particle formation that contribute to correspondingly high values of total particle concentrations and strongly seasonal total and CCN number concentrations (47, 52, 58, 80). New particle formation has been documented in the free troposphere, coastal regions, at ice edges, near clouds, and in the boundary layer if conditions are favorable (69). In the Antarctic and Arctic, particle formation events are typically connected to emissions from biological activity or iodine emissions from melting ice (58, 69). In the Arctic, where seasonal ice melt increases biological activity and bursts of new particle formation are initiated, a ~20% increase in CCN concentration is observed in summertime (81). Similar increases in new particle formation over the seasonal ice zone in the Antarctic summertime are observed along with the influence of recently formed free tropospheric particles on the region (58). Our analysis of ORCAS data (SFig. 3d) showed that SO N_d increases over retreating sea ice, suggesting the importance of particle formation and growth mechanisms associated with enhanced trace gas emissions. Synoptic activity in the SO likely mixes the pre-cursor gases and aerosol from this region further into the SO and, in combination with widespread ocean biological activity, influences N_d production across a wider expanse (Fig. 2a). If natural new particle formation mechanisms are not included in GCMs then it is likely that models systematically overestimate the strength of aerosol-cloud radiative forcing (82). This would result in an RF_{aci} that is too strong in models relative to observations, consistent with our constraint of the PPE sample by $\Delta N_{d(NH\text{-}SH)}$.

Discussion

The hemispheric contrast in oceanic N_d ($\Delta N_{d(NH\text{-}SH)}$) offers a constraint on changes in N_d between the preindustrial (PI) and present day (PD) ($\Delta N_{d(PD\text{-}PI)}$) and, by extension, on radiative forcing due to aerosol cloud interactions (RF_{aci}). Based on the observed $\Delta N_{d(NH\text{-}SH)}$ and output from GCMs, $\Delta N_{d(PD\text{-}PI)}$ is constrained to be between 8 and 24 cm^{-3}. RF_{aci} is constrained to be between -1.2 and -0.6 Wm^{-2}. This constraint on RF_{aci} agrees with the most probable range of -1.2 to -0.3 Wm^{-2} developed in Bellouin (3). The range developed in Bellouin (3) utilized observational studies relating aerosol variance to N_d variance. Our analysis is insensitive to aerosol observations and provides an important confirmation of this range using a different approach. Our analysis also suggests that the weaker RF_{aci} in the Bellouin (3) range is not consistent with observations. However, an important caveat to this study and other studies seeking to offer an observational constraint on GCM behavior using a single criterion is that it may result in an overly tight constraint on model behavior due to structural uncertainties in the GCM (45, 83). Future analysis will combine the hemispheric contrast in N_d with other constraints on model behavior to reinforce the robustness of our hemispheric constraint.

A key finding of this study is that models generally simulate larger hemispheric N_d differences than are observed. Observed $\Delta N_{d(NH\text{-}SH)}$ is relatively low partly due to high local summertime N_d over the SH, with N_d in the SO reach values near to those in outflows from North America and East Asia. Evaluation of in-situ data from cruises, flight campaigns, and stations on the Antarctic continent confirms the accuracy of remotely sensed SO N_d. Evaluation of SH CCN precipitation sinks demonstrates that high summertime N_d near Antarctica is in part due to low removal rates by precipitation scavenging on the poleward flank of the storm track. None of the GCMs surveyed here or the 235 original PPE ensemble members come near to reproducing the high near-Antarctic values in summertime (Fig. 1, individual models and PPE members shown in Fig. S1 and Fig. S2, respectively), suggesting models are missing key processes and/or emission sources important for CCN near Antarctica and potentially across the SH.

Ultimately, N_d is the variable that controls aerosol-cloud interactions (aci) in liquid clouds. This quantity is the product of aerosol emissions, removal, transport, processing, and nucleation, and it serves as a key assessment of GCM skill in portraying aci. This reinforces the need to continue to create N_d datasets from new satellites and in new ways. We propose that future evaluations of GCM aerosol-cloud interactions use the information contained within the contrast between pristine and polluted regions as an important test of realism in addition to evaluation of predicted N_d within anthropogenically-perturbed regions.

Materials and Methods

In this paper we contrast N_d predicted by GCMs with remotely sensed and *in situ* observations. N_d is always presented in-cloud, not averaged across cloudy and cloud-free regions. The central observational data set used in this study is MODIS C5.1 utilizing the 3.7 μm channel (84) during the period 2003-2015 (85). The calculation of N_d from MODIS observations of cloud optical depth and cloud droplet effective radius is not always reliable and the retrieval criterion presented in (86) are used to select for the most robust observations of N_d. Briefly, these criteria are that solar zenith angles are below 65°; cloud tops are within 3.2 km of the surface; and liquid cloud fractions are greater than 80% in a 1°x1° region (28, 86, 87). Data are filtered using these criteria based on individual Level-2 swaths (as opposed to daily averages) that have been averaged to 1°x1°.

Satellite retrievals in the SO are evaluated using observations from a variety of campaigns and ground stations. *In situ* CCN observations from McMurdo Station (48) and King Sejong Station (47) are drawn from the reported monthly and seasonal mean values in the literature. MODIS N_d for these regions is shown averaged across a 4° box centered at the respective stations (Fig. 3a). RITS total aerosol concentration was obtained from data provided to the Global Aerosol Synthesis and Science Project (GASSP) (88). ORCAS N_d data measured between the surface and 3 km is obtained from the Earth Observing Laboratory (EOL) at the National Center for Atmospheric Research (NCAR) (89). Sea ice cover was interpolated to the ORCAS flight track. The sea ice cover used in this analysis was from the Operational Sea Surface Temperature and Sea Ice Analysis (OSTIA) provided with the MERRA2 data product (59). The N_d observed by MODIS as a function of sea ice or open water was compared to the observations from ORCAS. For the comparison in Fig. 3d, MODIS N_d from 2003-2015 was restricted to only the days of the year and 1° regions where ORCAS measured N_d.

The GCM N_d examined in this study is provided by models participating in the Aerocom phase II indirect experiment (31); sensitivity experiments conducted in the development of HadGEM3-GA7.1 (32); and a perturbed parameter ensemble (PPE) within HadGEM3-GA4-UKCA (23). The Aerocom phase II models considered are CAM5, CAM5-PNNL, CAM5-CLUBB, CAM5-MG2, CAM5-CLUBB-MG2, ECHAM6.1.0-HAM2.2, SPRINTARS, and SPRINTARSKK. The model variants of the UM examined in Mulcahy*, et al.* (32) shown here are GA7.0, GA7.1, GA7.0_dms (DMS in sea water set to 170% of climatology), GA7.0_act (changes to the activation scheme), and GA7.0_comb (GA7.1 with no cloud tunings).

Multi-model ensembles (such as Aerocom) are invaluable for quantifying the magnitude of differences between models due to choices of physical process representations. However, this type of ensemble neglects the uncertainty within individual models. Perturbed parameter ensembles (PPEs) provide a useful means of quantifying single model uncertainty (90), however they neglect uncertainty caused by particular choices of process representations. We represent single model uncertainty using output from a PPE of the HadGEM-GA4-UKCA global climate model. In this PPE, 26 aerosol process, emission, and deposition parameters were simultaneously perturbed, allowing for assessment of a broad range of model behavior (Fig. S2). The PPE contains 235 model variants, each with a unique combination of the parameter values. Each PPE member simulated PD N_d resolved in space and time, PI global-mean N_d, and top-of-the-atmosphere radiative fluxes (used to calculate RF_{aci}). Horizontal winds and temperature fields were relaxed (91) towards 2008 meteorology from the European Centre for Medium-Range Weather Forecasts (ECMWF) ERA-Interim reanalyses and forced with year 2008 anthropogenic aerosol emissions from the MACCity emission inventory (92). To quantify uncertainty in changes over the industrial period, each of the 235 simulations has a partner simulation with identical parameter values, but with anthropogenic emissions from 1850 prescribed instead of PD emissions. The model was configured so that the first indirect effect of aerosols can be quantified in the absence of aerosol-cloud adjustments. Variations in N_d over the ensemble are caused entirely by differences in aerosol size distributions due to combinations of the 26 parameter values. We use the 235 member PPE to build statistical emulators of N_d and RF_{aci}. A sample of one million model variants (parameter combinations) is drawn from the emulator for each variable (33). Creation of the emulator assumes trapezoidal priors developed using expert solicitation (23). This makes the sample members more centralized in the multi-dimensional parameter space compared to the uniform priors assumed in earlier works (42, 45, 46, 93). If these uniform priors, which assume the entire range for all parameters are equally likely, are used in our analysis instead, the range of possible RF_{aci} consistent with observed $\Delta N_{d(NH\text{-}SH)}$ is between -1.4 and -0.5 Wm^{-2} (Fig. S6).

Hemispheric contrast in N_d ($\Delta N_{d(NH\text{-}SH)}$) is calculated as the difference in the annual mean of the area-weighted N_d concentrations over oceans 30-60°N and 30-60°S. N_d data in months and latitudes where MODIS observations are unavailable are removed from the GCM data before calculating the hemispheric contrast to avoid biases in comparing observations from MODIS and modeled N_d. The region 30°S-30°N is excluded because the retrieval of N_d by MODIS in convection is less robust (28). The 95% confidence on the hemispheric contrast was calculated by taking the standard error in the annual hemispheric contrast in the years 2003-2015 and assuming a normal distribution. We expect that this is an underestimation of the uncertainty in the observation but do not have an additional, global N_d dataset to use to estimate a more complete uncertainty. By examining the difference between hemispheres, we expect any systematic bias in the observations will be reduced.

The best fit line relating $\Delta N_{d(NH\text{-}SH)}$ to $\Delta N_{d(PD\text{-}PI)}$ and RF_{aci} was calculated using least-squares regression on the PPE sample members. The prediction band on the best fit line was used to quantify the possible range of N_d and RF_{aci} because all PPE sample members are considered to be equally valid representations of the real world. The prediction band about the best fit line was calculated by fitting the 95th percentile of PPE members in 30 quantiles of hemispheric contrast.

To quantitatively estimate the impact of marine boundary layer (MBL) precipitation on the seasonal climatology of N_d over the SO, we use the source and sink aerosol budget model developed in Wood, Leon, Lebsock, Snider and Clarke (71), hereafter W12. The model was developed for use over those parts of the global oceans where cloud condensation nuclei concentration loss rates are driven primarily by coalescence scavenging in MBL cloud systems (94). Modeled mean MBL CCN estimates from the model appropriate for describing the monthly mean climatology of N_d were shown to agree well with the observed N_d off the coast of Chile (71) and between California and Hawaii (95).

We apply the W12 model to estimate the impact of MBL cloud precipitation on the summertime meridional gradient of N_d over the SO. Using the equilibrium number concentration from the model (W12 eq. 2), we construct a ratio between N_d with precipitation loss and N_d computed with no precipitation loss. This is found to be inversely proportional to the precipitation rate (variables defined and values assumed as in W12):

$$\frac{N_d(precip)}{N_d(no\ precip)} = \frac{\left(N_{FT}+\frac{F(\sigma)U_{10}^{3.41}}{Dz_i}\right)\Big/\left(1+\frac{hKP_{CB}}{Dz_i}\right)}{\left(N_{FT}+\frac{F(\sigma)U_{10}^{3.41}}{Dz_i}\right)} = \left(1+\frac{hKP_{CB}}{Dz_i}\right)^{-1} \qquad \text{Eq. 1}$$

We estimate the coalescence-scavenging sink using the CloudSat-derived precipitation rate product (96). This product attempts to estimate precipitation from all cloud systems, not only those arising from MBL clouds. Previous applications of this model examined the eastern ocean subtropical systems (71, 95) where precipitation was primarily derived from low cloud systems. In contrast, across the SO there is considerably more precipitation emanating from deeper precipitating systems (97). This is accounted for by only considering CloudSat precipitation estimates with detectable echo tops below 3 km altitude. This attempts to ensure that only precipitation that has a significant contribution to the coalescence scavenging of MBL CCN is used as input to the CCN and N_d budget models. This choice is based on data from the Azores, which straddles the boundary between the subtropics and the midlatitudes (~40ºN), showing that between 15% and 30% of all precipitation reaching the surface originated from clouds with tops below 3 km (98). Similarly, between 30°S and 70°S, with weak dependence on latitude, we find that 15-35% of all precipitation reaching the surface originates from clouds with tops below ~3 km (Fig. S5a-e).

Acknowledgments

We thank Toshihiko Takemura for their help in interpreting data from the SPRINTARS model. ORCAS Campaign data provided by NCAR/EOL under the sponsorship of the National Science Foundation (https://data.eol.ucar.edu/). FB partly funded by Vetenskapsrådet grant no. 2018-04274. DTM and PRF acknowledge support from the PRIMAVERA project funded by the European Union's Horizon 2020 program under grant agreement no. 641727.

We acknowledge funding from NERC under grants AEROS, ACID-PRUF, GASSP and A-CURE (NE/G006172/1, NE/I020059/1, NE/J024252/1 and NE/P013406/1) and the European Union ACTRIS-2 project under grant 262254. This work and its contributors (LR and KC) were supported by the UK-China Research & Innovation Partnership Fund through the Met Office Climate Science for Service Partnership (CSSP) China as part of the Newton Fund. KS received funding from the National Centre for Atmospheric Science (NCAS), one of the UK Natural Environment Research Council (NERC) research centers via the ACSIS long-term science programme on the Atlantic climate system. KC is currently a Royal Society Wolfson Merit Award holder. DWP acknowledges funding from the Natural Environment Research Council (NERC) NE/P013406/1 (A-CURE) and NE/L013746/1 (CLARIFY) projects. DPG was funded by the NERC funded ACSIS programme via NCAS. JPM was supported by the Met Office Hadley Centre Climate Programme funded by BEIS and Defra (Grant Number GA01101). DTM and PRF acknowledge support from the PRIMAVERA project, funded by the European Union's Horizon 2020 programme, Grant Agreement no. 641727.

References

1. M. O. Andreae, C. D. Jones, P. M. Cox, Strong present-day aerosol cooling implies a hot future. *Nature* **435**, 1187-1190 (2005).
2. P. M. Forster, Inference of Climate Sensitivity from Analysis of Earth's Energy Budget. *Annual Review of Earth and Planetary Sciences* **44**, 85-106 (2016).
3. N. Bellouin, Quaas, J., Gryspeerdt, E., Kinne, S., Stier, P., Watson-Parris, D., Boucher, O., Carslaw, K. S., Christensen, M., Daniau, A.-L., Dufresne, J.-L., Feingold, G., Fiedler, S., Forster, P., Gettelman, A., Haywood, J.M., Lohmann, U., Malavelle, F., Mauritsen, T., McCoy, D.T., Myhre, G., Muelmenstaedt, J., Neubauer, D., Possner, A., Rugenstein, M., Sato, Y., Schulz, M., Schwartz, S.E., Sourdeval, O., Storelvmo, T., Toll, V., Winker, D. and Stevens, B., Bounding global aerosol radiative forcing of climate change. *Reviews of Geophysics* (2019).
4. S. Twomey, The Influence of Pollution on the Shortwave Albedo of Clouds. *Journal of the Atmospheric Sciences* **34**, 1149-1152 (1977).
5. B. A. Albrecht, Aerosols, cloud microphysics, and fractional cloudiness. *Science* **245**, 1227-1230 (1989).
6. O. Boucher, D. Randall, P. Artaxo, C. Bretherton, G. Feingold, P. Forster, V.-M. Kerminen, Y. Kondo, H. Liao, U. Lohmann, P. Rasch, S.K. Satheesh, S. Sherwood, B. Stevens and X.Y. Zhang, (2013) Clouds and Aerosols. in *Climate Change 2013: The Physical Science Basis. Contribution of Working Group I to the Fifth Assessment Report of the Intergovernmental Panel on Climate Change*, ed T. F. [Stocker, D. Qin, G.-K. Plattner, M. Tignor, S.K. Allen, J. Boschung, A. Nauels, Y. Xia, V. Bex and P.M. Midgley (eds.)] (Cambridge University Press, Cambridge, United Kingdom and New York, NY, USA.).
7. F. F. Malavelle *et al.*, Strong constraints on aerosol–cloud interactions from volcanic eruptions. *Nature* **546**, 485-491 (2017).
8. V. Toll, M. Christensen, S. Gassó, N. Bellouin, Volcano and Ship Tracks Indicate Excessive Aerosol-Induced Cloud Water Increases in a Climate Model. *Geophysical Research Letters* **44**, 12,492-412,500 (2017).
9. Y. Sato *et al.*, Aerosol effects on cloud water amounts were successfully simulated by a global cloud-system resolving model. *Nature Communications* **9**, 985 (2018).

10. F.-M. Bender, L. Frey, D. T. McCoy, D. P. Grosvenor, J. K. Mohrmann, Assessment of aerosol–cloud–radiation correlations in satellite observations, climate models and reanalysis. *Climate Dynamics* **52**, 4371-4392 (2019).
11. V. Toll, M. Christensen, J. Quaas, N. Bellouin, Weak average liquid-cloud-water response to anthropogenic aerosols. *Nature* **572**, 51-55 (2019).
12. E. Gryspeerdt *et al.*, Constraining the aerosol influence on cloud liquid water path. *Atmos. Chem. Phys.* **19**, 5331-5347 (2019).
13. E. Gryspeerdt, J. Quaas, N. Bellouin, Constraining the aerosol influence on cloud fraction. *Journal of Geophysical Research: Atmospheres* 10.1002/2015JD023744, n/a-n/a (2016).
14. K. S. Carslaw *et al.*, Large contribution of natural aerosols to uncertainty in indirect forcing. *Nature* **503**, 67-+ (2013).
15. L. A. Regayre *et al.*, Uncertainty in the magnitude of aerosol-cloud radiative forcing over recent decades. *Geophysical Research Letters* **41**, 9040-9049 (2014).
16. D. S. Hamilton *et al.*, Occurrence of pristine aerosol environments on a polluted planet. *Proceedings of the National Academy of Sciences* **111**, 18466-18471 (2014).
17. Q. Han, W. B. Rossow, A. A. Lacis, Near-Global Survey of Effective Droplet Radii in Liquid Water Clouds Using ISCCP Data. **7**, 465-497 (1994).
18. Y. Feng, V. Ramanathan, Investigation of aerosol–cloud interactions using a chemical transport model constrained by satellite observations. *Tellus B: Chemical and Physical Meteorology* **62**, 69-86 (2010).
19. O. Boucher, U. Lohmann, The sulfate-CCN-cloud albedo effect. *Tellus B* **47**, 281-300 (1995).
20. C. Seethala, A. Horvath, Global assessment of AMSR-E and MODIS cloud liquid water path retrievals in warm oceanic clouds. *Journal of Geophysical Research-Atmospheres* **115** (2010).
21. D. P. Grosvenor *et al.*, Remote Sensing of Droplet Number Concentration in Warm Clouds: A Review of the Current State of Knowledge and Perspectives. *Rev Geophys* **56**, 409-453 (2018).
22. R. Wood, Stratocumulus Clouds. *Monthly Weather Review* **140**, 2373-2423 (2012).
23. M. Yoshioka *et al.*, Ensembles of Global Climate Model Variants Designed for the Quantification and Constraint of Uncertainty in Aerosols and Their Radiative Forcing. *J. Adv. Model. Earth Syst.* 10.1029/2019ms001628 (2019).
24. D. Painemal, P. Minnis, J. K. Ayers, L. O'Neill, GOES-10 microphysical retrievals in marine warm clouds: Multi-instrument validation and daytime cycle over the southeast Pacific. *Journal of Geophysical Research: Atmospheres* **117**, n/a-n/a (2012).
25. M. K. Witte *et al.*, MODIS Retrievals of Cloud Effective Radius in Marine Stratocumulus Exhibit No Significant Bias. *Geophysical Research Letters* **45**, 10,656-610,664 (2018).
26. D. Painemal, P. Zuidema, Assessment of MODIS cloud effective radius and optical thickness retrievals over the Southeast Pacific with VOCALS-REx in situ measurements. *Journal of Geophysical Research-Atmospheres* **116** (2011).
27. R. Bennartz, J. Rausch, Global and regional estimates of warm cloud droplet number concentration based on 13 years of AQUA-MODIS observations. *Atmos. Chem. Phys.* **17**, 9815-9836 (2017).

28. D. P. Grosvenor *et al.*, Remote Sensing of Droplet Number Concentration in Warm Clouds: A Review of the Current State of Knowledge and Perspectives. *Reviews of Geophysics* **56**, 409-453 (2018).
29. D. T. McCoy *et al.*, Predicting decadal trends in cloud droplet number concentration using reanalysis and satellite data. *Atmospheric Chemistry and Physics* **18**, 2035-2047 (2018).
30. E. Ahn, Y. Huang, S. T. Siems, M. J. Manton, A Comparison of Cloud Microphysical Properties Derived From MODIS and CALIPSO With In Situ Measurements Over the Wintertime Southern Ocean. *Journal of Geophysical Research: Atmospheres* **123**, 11,120-111,140 (2018).
31. S. Ghan *et al.*, Challenges in constraining anthropogenic aerosol effects on cloud radiative forcing using present-day spatiotemporal variability. *Proceedings of the National Academy of Sciences* 10.1073/pnas.1514036113 (2016).
32. J. P. Mulcahy *et al.*, Improved Aerosol Processes and Effective Radiative Forcing in HadGEM3 and UKESM1. *J. Adv. Model. Earth Syst.* **10**, 2786-2805 (2018).
33. D. Watson-Parris *et al.*, Constraining uncertainty in aerosol direct forcing. *Geophysical Research Letters (Submitted)* (2019).
34. G. P. Ayers, J. L. Gras, Seasonal relationship between cloud condensation nuclei and aerosol methanesulphonate in marine air. *Nature* **353**, 834-835 (1991).
35. D. T. McCoy *et al.*, Natural aerosols explain seasonal and spatial patterns of Southern Ocean cloud albedo. *Sci Adv* **1**, e1500157 (2015).
36. G. Zheng *et al.*, Marine boundary layer aerosol in the eastern North Atlantic: seasonal variations and key controlling processes. *Atmospheric Chemistry and Physics* **18**, 17615-17635 (2018).
37. K. J. Sanchez *et al.*, Substantial Seasonal Contribution of Observed Biogenic Sulfate Particles to Cloud Condensation Nuclei. *Scientific Reports* **8**, 3235 (2018).
38. M. Schulz *et al.*, Radiative forcing by aerosols as derived from the AeroCom present-day and pre-industrial simulations. *Atmos. Chem. Phys.* **6**, 5225-5246 (2006).
39. D. S. Hamilton *et al.*, Reassessment of pre-industrial fire emissions strongly affects anthropogenic aerosol forcing. *Nature communications* **9**, 3182 (2018).
40. K. S. Carslaw *et al.*, Aerosols in the Pre-industrial Atmosphere. *Current Climate Change Reports* **3**, 1-15 (2017).
41. P. Stier, J. Feichter, S. Kloster, E. Vignati, J. Wilson, Emission-induced nonlinearities in the global aerosol system: Results from the ECHAM5-HAM aerosol-climate model. *Journal of climate* **19**, 3845-3862 (2006).
42. L. A. Regayre *et al.*, Aerosol and physical atmosphere model parameters are both important sources of uncertainty in aerosol ERF. *Atmospheric Chemistry and Physics* **18**, 9975-10006 (2018).
43. K. S. Carslaw, L. A. Lee, L. A. Regayre, J. S. Johnson (2018) Climate models are uncertain, but we can do something about it. in *Eos*.
44. L. A. Lee, C. L. Reddington, K. S. Carslaw, On the relationship between aerosol model uncertainty and radiative forcing uncertainty. *Proc Natl Acad Sci U S A* **113**, 5820-5827 (2016).
45. J. S. Johnson *et al.*, The importance of comprehensive parameter sampling and multiple observations for robust constraint of aerosol radiative forcing. *Atmospheric Chemistry and Physics* **18**, 13031-13053 (2018).

46. L. A. Regayre *et al.*, 10.5194/acp-2019-1085.
47. J. Kim *et al.*, Seasonal variations in physical characteristics of aerosol particles at the King Sejong Station, Antarctic Peninsula. *Atmospheric Chemistry and Physics* **17**, 12985-12999 (2017).
48. J. Liu *et al.*, High summertime aerosol organic functional group concentrations from marine and seabird sources at Ross Island, Antarctica, during AWARE. *Atmospheric Chemistry and Physics* **18**, 8571-8587 (2018).
49. E. Jang *et al.*, New particle formation events observed at the King Sejong Station, Antarctic Peninsula – Part 2: Link with the oceanic biological activities. *Atmospheric Chemistry and Physics* **19**, 7595-7608 (2019).
50. J. Kim *et al.*, New particle formation events observed at King Sejong Station, Antarctic Peninsula – Part 1: Physical characteristics and contribution to cloud condensation nuclei. *Atmospheric Chemistry and Physics* **19**, 7583-7594 (2019).
51. J. Schmale *et al.*, Overview of the Antarctic Circumnavigation Expedition: Study of Preindustrial-like Aerosols and Their Climate Effects (ACE-SPACE). *Bulletin of the American Meteorological Society* **100**, 2260-2283 (2019).
52. R. S. Humphries *et al.*, Unexpectedly high ultrafine aerosol concentrations above East Antarctic sea ice. *Atmos. Chem. Phys.* **16**, 2185-2206 (2016).
53. D. S. Covert, V. N. Kapustin, T. S. Bates, P. K. Quinn, Physical properties of marine boundary layer aerosol particles of the mid-Pacific in relation to sources and meteorological transport. **101**, 6919-6930 (1996).
54. P. K. Quinn, V. N. Kapustin, T. S. Bates, D. S. Covert, Chemical and optical properties of marine boundary layer aerosol particles of the mid-Pacific in relation to sources and meteorological transport. *Journal of Geophysical Research: Atmospheres* **101**, 6931-6951 (1996).
55. C. W. Sullivan, C. R. McClain, J. C. Comiso, W. O. Smith, Phytoplankton standing crops within an Antarctic ice edge assessed by satellite remote sensing. *Journal of Geophysical Research* **93**, 12487 (1988).
56. W. O. Smith, D. M. Nelson, Importance of Ice Edge Phytoplankton Production in the Southern Ocean. *BioScience* **36**, 251-257 (1986).
57. K. Petrou *et al.*, Southern Ocean phytoplankton physiology in a changing climate. *J Plant Physiol* **203**, 135-150 (2016).
58. T. Lachlan-Cope *et al.*, 10.5194/acp-2019-847.
59. C. J. Donlon *et al.*, The Operational Sea Surface Temperature and Sea Ice Analysis (OSTIA) system. *Remote Sensing of Environment* **116**, 140-158 (2012).
60. T. Lachlan-Cope, C. Listowski, S. O'Shea, The microphysics of clouds over the Antarctic Peninsula – Part 1: Observations. *Atmos. Chem. Phys.* **16**, 15605-15617 (2016).
61. H. Korhonen, K. S. Carslaw, D. V. Spracklen, G. W. Mann, M. T. Woodhouse, Influence of oceanic dimethyl sulfide emissions on cloud condensation nuclei concentrations and seasonality over the remote Southern Hemisphere oceans: A global model study. *Journal of Geophysical Research-Atmospheres* **113** (2008).
62. S. M. Burrows *et al.*, A physically based framework for modeling the organic fractionation of sea spray aerosol from bubble film Langmuir equilibria. *Atmos. Chem. Phys.* **14**, 13601-13629 (2014).
63. J. W. Fitzgerald, Marine aerosols: A review. *Atmospheric Environment. Part A. General Topics* **25**, 533-545 (1991).

64. S. N. Pandis, L. M. Russell, J. H. Seinfeld, The relationship between DMS flux and CCN concentration in remote marine regions. *Journal of Geophysical Research* **99**, 16945-16957 (1994).
65. G. P. Ayers, J. M. Cainey, R. W. Gillett, J. P. Ivey, Atmospheric sulphur and cloud condensation nuclei in marine air in the Southern Hemisphere. *Philosophical Transactions of the Royal Society of London Series B-Biological Sciences* **352**, 203-211 (1997).
66. G. P. Ayers, R. W. Gillett, DMS and its oxidation products in the remote marine atmosphere: implications for climate and atmospheric chemistry. *Journal of Sea Research* **43**, 275-286 (2000).
67. D. Katoshevski, A. Nenes, J. H. Seinfeld, A study of processes that govern the maintenance of aerosols in the marine boundary layer. *Journal of Aerosol Science* **30**, 503-532 (1999).
68. A. L. Hodshire *et al.*, The potential role of methanesulfonic acid (MSA) in aerosol formation and growth and the associated radiative forcings. *Atmos. Chem. Phys.* **19**, 3137-3160 (2019).
69. V.-M. Kerminen *et al.*, Atmospheric new particle formation and growth: review of field observations. *Environmental Research Letters* **13** (2018).
70. E. M. Dunne *et al.*, Global atmospheric particle formation from CERN CLOUD measurements. *Science* **354**, 1119-1124 (2016).
71. R. Wood, D. Leon, M. Lebsock, J. Snider, A. D. Clarke, Precipitation driving of droplet concentration variability in marine low clouds. *Journal of Geophysical Research-Atmospheres* **117** (2012).
72. B. J. Hoskins, K. I. Hodges, A New Perspective on Southern Hemisphere Storm Tracks. *Journal of Climate* **18**, 4108-4129 (2005).
73. R. S. Humphries *et al.*, Unexpectedly high ultrafine aerosol concentrations above East Antarctic sea ice. *Atmospheric Chemistry and Physics* **16**, 2185-2206 (2016).
74. K. M. Chan, R. Wood, The seasonal cycle of planetary boundary layer depth determined using COSMIC radio occultation data. *Journal of Geophysical Research: Atmospheres* **118**, 12,422-412,434 (2013).
75. N. Meskhidze, A. Nenes, Phytoplankton and Cloudiness in the Southern Ocean. *Science* **314**, 1419-1423 (2006).
76. G. L. Stephens *et al.*, Dreary state of precipitation in global models. *Journal of Geophysical Research: Atmospheres* **115** (2010).
77. A. Lana *et al.*, An updated climatology of surface dimethlysulfide concentrations and emission fluxes in the global ocean. *Global Biogeochemical Cycles* **25** (2011).
78. A. Bodas-Salcedo *et al.*, Strong dependence of atmospheric feedbacks on mixed-phase microphysics and aerosol-cloud interactions in HadGEM3. *J. Adv. Model. Earth Syst.* **11**, 1735-1758 (2019).
79. L. E. Revell *et al.*, 10.5194/acp-2019-629.
80. P. Herenz *et al.*, CCN measurements at the Princess Elisabeth Antarctica research station during three austral summers. *Atmospheric Chemistry and Physics* **19**, 275-294 (2019).
81. M. Dall Osto *et al.*, Arctic sea ice melt leads to atmospheric new particle formation. *Sci Rep* **7**, 3318 (2017).

82. H. Gordon *et al.*, Reduced anthropogenic aerosol radiative forcing caused by biogenic new particle formation. *Proceedings of the National Academy of Sciences* **113**, 12053-12058 (2016).
83. L. A. Regayre *et al.*, Aerosol and physical atmosphere model parameters are both important sources of uncertainty in aerosol ERF. *Atmospheric Chemistry and Physics* **18**, 9975-10006 (2018).
84. M. D. King *et al.*, Cloud and aerosol properties, precipitable water, and profiles of temperature and water vapor from MODIS. *Geoscience and Remote Sensing, IEEE Transactions on* **41**, 442-458 (2003).
85. D. P. W. Grosvenor, R., Daily MODIS (MODerate Imaging Spectroradiometer) derived cloud droplet number concentration global dataset for 2003-2015. Centre for Environmental Data Analysis. http://catalogue.ceda.ac.uk/uuid/cf97ccc802d348ec8a3b6f2995dfbbff.
86. D. P. Grosvenor, R. Wood, The effect of solar zenith angle on MODIS cloud optical and microphysical retrievals within marine liquid water clouds. *Atmospheric Chemistry and Physics* **14**, 7291-7321 (2014).
87. D. P. Grosvenor, O. Sourdeval, R. Wood, Parameterizing cloud top effective radii from satellite retrieved values, accounting for vertical photon transport: quantification and correction of the resulting bias in droplet concentration and liquid water path retrievals. *Atmospheric Measurement Techniques* **11**, 4273-4289 (2018).
88. C. Reddington *et al.*, The Global Aerosol Synthesis and Science Project (GASSP): measurements and modelling to reduce uncertainty. (2017).
89. U. N.-E. O. Laboratory, Low Rate (LRT - 1 sps) Navigation, State Parameter, and Microphysics Flight-Level Data. Version 1.1.
90. M. Collins *et al.*, Climate model errors, feedbacks and forcings: a comparison of perturbed physics and multi-model ensembles. *Climate Dynamics* **36**, 1737-1766 (2010).
91. P. J. Telford, P. Braesicke, O. Morgenstern, J. A. Pyle, Technical Note: Description and assessment of a nudged version of the new dynamics Unified Model. *Atmos. Chem. Phys.* **8**, 1701-1712 (2008).
92. C. Granier *et al.*, Evolution of anthropogenic and biomass burning emissions of air pollutants at global and regional scales during the 1980–2010 period. *Climatic Change* **109**, 163-190 (2011).
93. J. S. Johnson *et al.*, 10.5194/acp-2019-834.
94. R. Wood, Rate of loss of cloud droplets by coalescence in warm clouds. *Journal of Geophysical Research: Atmospheres* **111** (2006).
95. J. Mohrmann, R. Wood, J. McGibbon, R. Eastman, E. Luke, Drivers of Seasonal Variability in Marine Boundary Layer Aerosol Number Concentration Investigated Using a Steady State Approach. *Journal of Geophysical Research: Atmospheres* **123**, 1097-1112 (2018).
96. J. M. Haynes *et al.*, Rainfall retrieval over the ocean with spaceborne W-band radar. *Journal of Geophysical Research: Atmospheres* **114** (2009).
97. Z. Wang, S. T. Siems, D. Belusic, M. J. Manton, Y. Huang, A climatology of the precipitation over the Southern Ocean as observed at Macquarie Island. *Journal of Applied Meteorology and Climatology* **54**, 2321-2337 (2015).
98. R. Wood *et al.*, Clouds, aerosols, and precipitation in the marine boundary layer: An arm mobile facility deployment. *Bulletin of the American Meteorological Society* **96**, 419-440 (2015).

Figures and Tables

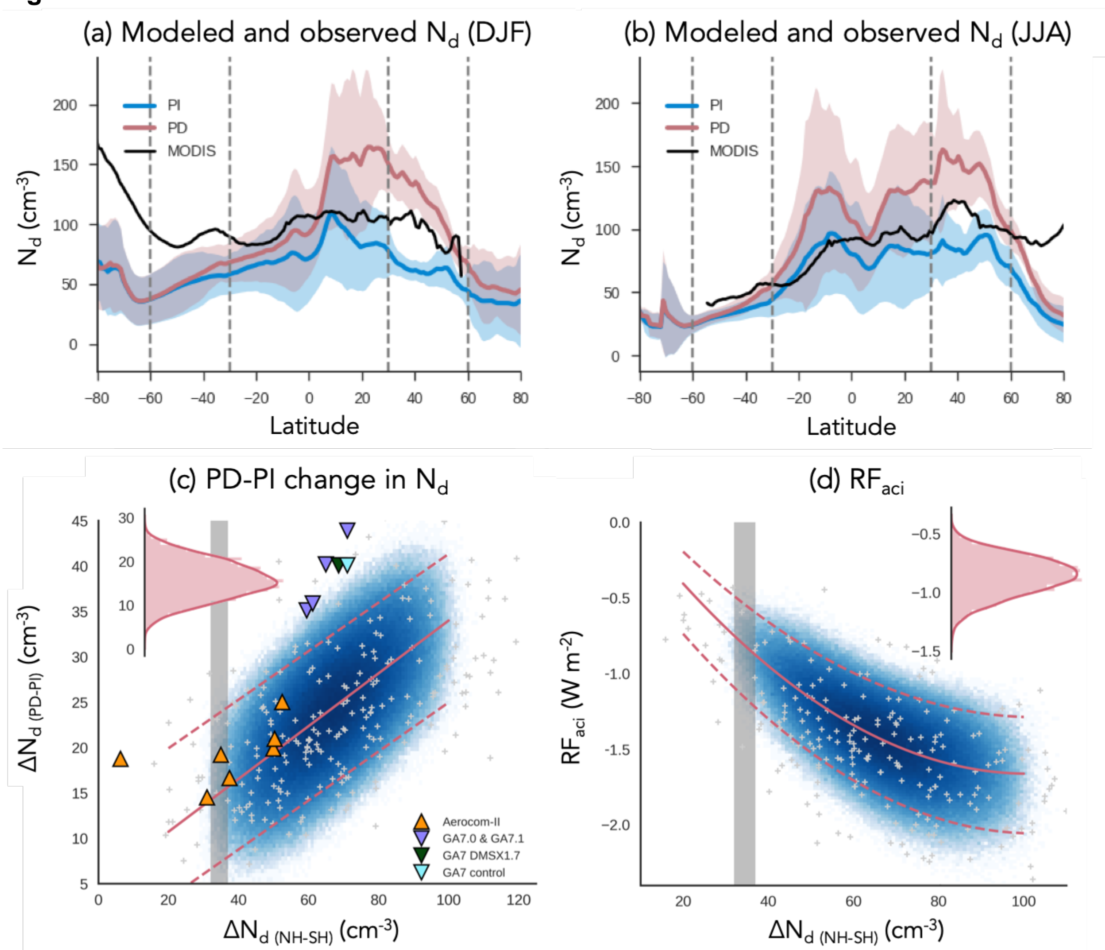

Figure 1. Constraints on aerosol-cloud interactions (*aci*) from observed hemispheric contrast in N_d over oceans ($N_{d(NH-SH)}$). (a,b) Oceanic Pre-Industrial (PI, blue) and Present Day (PD, red) N_d modeled by Aerocom-II models and HadGEM3-GA7.1 development models. Thick lines show the multi-model mean, corresponding shading shows the standard deviation across models. Data from DJF and JJA are shown separately in (a) and (b). In Southern Ocean winter the Aerocom-II NCAR models are missing data due to lack of low, liquid cloud, leading to discontinuity in the multi-model mean at 70°S. Zonal means from each model are shown in Fig. S1. $N_{d(NH-SH)}$ is calculated as the difference in annual, area-weighted mean N_d over the ocean between 30-60°N and 30-60°S (averaging boundaries shown as vertical dashed lines). (c) Change in oceanic N_d between the PI and PD ($\Delta N_{d(PD-PI)}$) as a function of $N_{d(NH-SH)}$ in PPE members (gray crosses for individual model members, blue shading for N_d values sampled from a statistical emulator), in Aerocom-II (orange triangles), and HadGEM-GA7.1 development models (purple, blue, and dark green triangles). HadGEM-GA7.0 with enhanced DMS is shown in dark green and the control HadGEM-GA7.0 in blue. The linear fit to the PPE data and 95% prediction bands on the fit are shown as red solid and dashed lines. The 95% confidence on the interannual range of MODIS observations is shown in gray. (d) as in (c) but showing the relation between RF_{aci} and the hemispheric contrast calculated from the PPE sample members along with a second-order polynomial fit between $N_{d(NH-SH)}$ and RF_{aci}. The PDF of the emulated PPE member values within the observationally constrained range of $N_{d(NH-SH)}$ is shown in the top left for $\Delta N_{d(PD-PI)}$ (c) and top right for RF_{aci} (d).

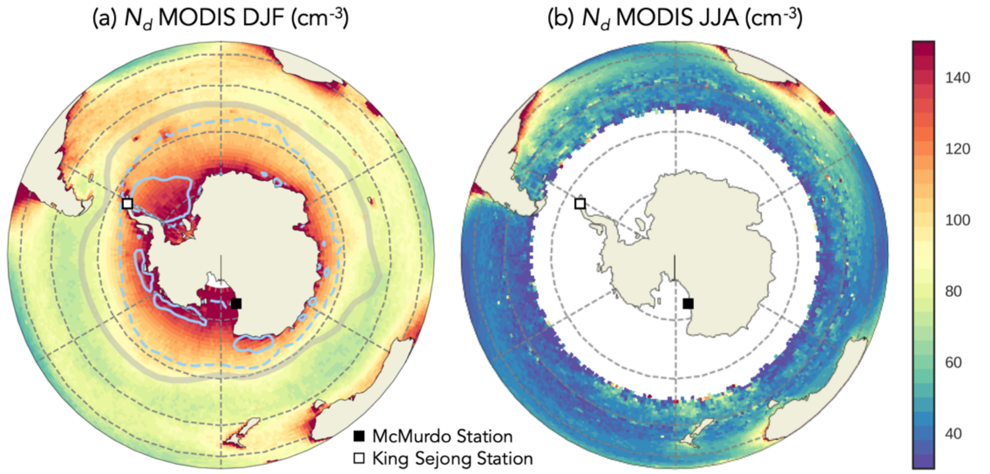

Figure 2. Mean N_d from MODIS in summer (a, DJF) and winter (b, JJA). Seasonal-mean sea ice contours from OSTIA fractional sea ice are shown as dashed (1%) and solid blue lines (50%). Locations are shown for McMurdo Station (48) (solid square) and King Sejong Station (47) (empty square). The position of the DJF lower tropospheric storm track (72) is shown with a gray line.

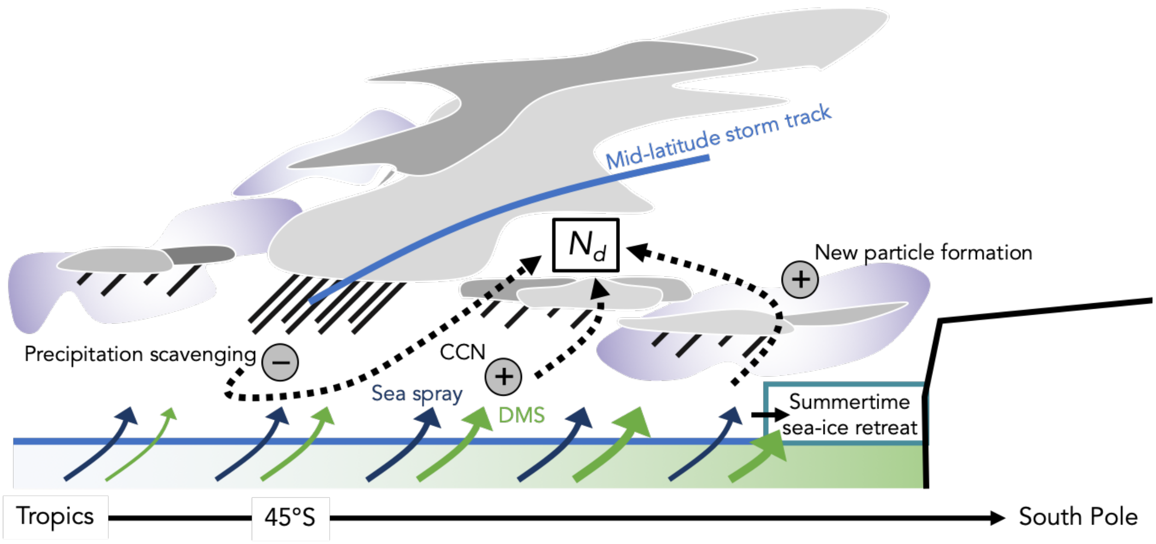

Figure 3. Schematic depicting some of the possible sources (+) and sinks (-) of N_d in the Southern Ocean. Approximate location of the climatological mid-latitude storm track is shown for reference.